

Leveraging Frequency Analysis for Deep Fake Image Recognition

Joel Frank¹ Thorsten Eisenhofer¹ Lea Schönherr¹ Asja Fischer¹ Dorothea Kolossa¹ Thorsten Holz¹

Abstract

Deep neural networks can generate images that are astonishingly realistic, so much so that it is often hard for humans to distinguish them from actual photos. These achievements have been largely made possible by Generative Adversarial Networks (GANs). While these *deep fake* images have been thoroughly investigated in the image domain—a classical approach from the area of image forensics—an analysis in the *frequency domain* has been missing so far.

In this paper, we address this shortcoming and our results reveal that in frequency space, GAN-generated images exhibit severe artifacts that can be easily identified. We perform a comprehensive analysis, showing that these artifacts are consistent across different neural network architectures, data sets, and resolutions. In a further investigation, we demonstrate that these artifacts are caused by upsampling operations found in all current GAN architectures, indicating a structural and fundamental problem in the way images are generated via GANs. Based on this analysis, we demonstrate how the frequency representation can be used to identify deep fake images in an automated way, surpassing state-of-the-art methods.

1. Introduction

GANs produce sample outputs—images, audio signals, or complete video sequences—that are astonishingly effective at fooling humans into believing their veracity (Fried et al., 2019; Karras et al., 2019; Kumar et al., 2019; Song et al., 2020). The difficulty of distinguishing these so-called *deep fakes* from real media is for example demonstrated at whichfaceisreal.com (West & Bergstrom, 2019), a website on which a user can see two different images: one from the Flicker-Faces-HQ data set and one generated by StyleGAN (Karras et al., 2019). The task is to decide which of

¹Ruhr-Universität Bochum, Horst Görz Institute for IT-Security, Bochum, Germany. Correspondence to: Joel Frank <joel.frank@rub.de>.

these two images is real. Even though humans generally do better than random guessing, players’ performance reportedly peaked at around 75% accuracy (Simonite, 2019).

At a time where fake news have become a practical problem and Internet information campaigns have started to influence democratic processes (Thompson & Lapowsky, 2017), developing automated detection methods is a crucial task. A worrying reminder is the example of Gabon’s president Ali Bongo: In late 2018, the president fell ill, not appearing in public for months. As the public grew weary, the government released a video of the president, only to be immediately labeled as a deep fake. Albeit never to be confirmed as such, one week later the military launched an unsuccessful coup, citing the video as part of the motivation (Hao, 2019).

Previous research on detecting GAN-generated images has either utilized large, complex convolutional networks directly trained in the image domain (Mo et al., 2018; Yu et al., 2019a; Tariq et al., 2019) or used hand-crafted features from the frequency domain (Marra et al., 2019; Valle et al., 2018). In contrast, we provide in this paper a comprehensive analysis of the frequency spectrum across multiple different GAN architectures and data sets. The surprising finding is that *all* GAN architectures exhibit severe artifacts in the frequency domain. Speculating that these artifacts stem from upsampling operations, we experiment with different upsampling techniques and identify patterns which are consistent with our earlier observations.

Based on these insights, we demonstrate that the frequency domain can be utilized for (i) separating real from fake images, as well as, (ii) identifying by which specific GAN a sample was generated. In the first case, we demonstrate that the artifacts are so severe that a linear separation of the data is possible in the frequency space. In the second case, we demonstrate that we can achieve higher accuracy, while simultaneously utilizing significantly less complex models, than state-of-the-art approaches (Yu et al., 2019a) (using roughly 1.9% of their parameters). Additionally, we demonstrate that classifiers trained in the frequency domain are more robust against common image perturbations (e.g., blurring or cropping). The code to reproduce our experiments and plots, as well as, all pre-trained models are available online at github.com/Syssec/DCTAnalysis.

In summary, our contributions are as follows:

- We perform a comprehensive frequency-domain analysis of images generated by various popular GANs, revealing severe artifacts common across different neural network architectures, data sets, and resolutions.
- We show in several experiments that these artifacts arise from upsampling operations employed in all current GAN architectures, hinting towards a structural problem on how generative neural networks that map from a low-dimensional latent space to a higher-dimensional input space are constructed.
- We demonstrate the effectiveness of employing frequency representations for detecting GAN-generated deep fake images by an empirical comparison against state-of-the-art approaches, showing that frequency-representation-based classifiers yield higher accuracy, while simultaneously needing significantly fewer parameters. Additionally, these classifiers prove to be more robust to common image perturbations.

2. Related Work

In the following, we present an overview of related work and discuss how our approach is connected to these.

Generative Adversarial Networks GANs (Goodfellow et al., 2014) have essentially established a new sub-field of modern machine learning research. As generative models, they aim at estimating the probability density distribution underlying the training data. Instead of employing standard approaches like likelihood maximization for training, they are based on the idea of defining a game between two competing models (usually neural networks): a generator and a classifier (also called discriminator). The generator is tasked with producing samples that look like training data, while the discriminator attempts to distinguish real from fake (i.e., generated) samples. These tasks can be translated into a min-max problem: a joint objective which is minimized w.r.t. the parameters of the generator and maximized w.r.t. the parameters of the discriminator.

Image Synthesis While there exists a huge variety of models for image generation (e.g. see van den Oord et al., 2017; Razavi et al., 2019), we will focus on images generated by GANs. The earliest breakthrough in generating images with GANs was the switch to Convolutional Neural Network (CNN) (Radford et al., 2016). While this might seem trivial today, it allowed GANs to outperform similar image synthesis methods at the time. In follow-up work, GAN research yielded a steady stream of innovations, which pushed the state-of-the-art further: training with labeled data (Mirza & Osindero, 2014; Salimans et al., 2016), utilizing the Wasserstein distance (Arjovsky et al., 2017;

Gulrajani et al., 2017; Petzka et al., 2018), spectral normalization (Miyato et al., 2018), progressive growing (Karras et al., 2018) or style mixing (Karras et al., 2019), and employing very large models (Brock et al., 2019), just to name a few examples.

Image Forensics Traditional image forensics uses the natural statistics of images to detect tampered media (Fridrich, 2009; Lyu, 2013). A common approach is steganalysis (Lukáš et al., 2006; Fridrich, 2009; Bestagini et al., 2013), where high-frequency residuals are used to detect manipulations. These traditional methods have recently been expanded by CNN-based methods (Bayar & Stamm, 2016; Bappy et al., 2017; Cozzolino et al., 2017; Zhou et al., 2018), which learn a more complex feature representation, improving the state-of-the-art for tampered media detection.

Prior work has utilized these findings for identifying GAN-generated images: Marra et al. provide a comparison of different steganalysis and CNN-based methods (Marra et al., 2018), several approaches use CNNs in the image domain (Mo et al., 2018; Yu et al., 2019a; Tariq et al., 2019), others use statistics in the image domain (McCloskey & Albright, 2018; Nataraj et al., 2019). Another type of systems have used handcrafted features from the frequency domain, namely, steganalysis-based features (Marra et al., 2019) and spectral centroids (Valle et al., 2018). In contrast, our method explores the entire frequency spectrum and we link our detection capabilities to fundamental shortcomings in the construction of modern generative neural networks.

3. Frequency Artifacts

While early GAN-generated images were easily distinguishable from real images, newer generations fool even human observers (Simonite, 2019). To facilitate the development of automated methods for recognizing fake images, we take inspiration from traditional image forensics (Lyu, 2013) and examine GAN-generated images in the frequency domain.

3.1. Preliminaries

We transform images into the frequency domain using the discrete cosine transform (DCT). The DCT expresses, much like the discrete Fourier transform, a finite sequence of data points as a sum of cosine functions oscillating at different frequencies. The DCT is commonly used in image processing due to its excellent energy compaction properties and its separability, which allows for efficient implementations. Together with a circular convolution-multiplication relationship (Wen-Hsiung Chen et al., 1977), it enables fast filtering. We use the type-II 2D-DCT, which is, for example, also used in JPEG compression (Fridrich, 2009).

More formally, let an input image be given by the matrix¹ $I \in \mathbb{R}^{N_1 \times N_2}$, where the entries (specifying the pixel values) are denoted by $I_{x,y}$, and its DCT-transformed representation by the matrix $D \in \mathbb{R}^{N_1 \times N_2}$. The 2D-DCT is given by a function $\mathcal{D} : \mathbb{R}^{N_1 \times N_2} \rightarrow \mathbb{R}^{N_1 \times N_2}$ that maps an image $I = \{I_{x,y}\}$ to its frequency representation $D = \{D_{k_x, k_y}\}$, where for $\forall k_x = 0, 1, 2, \dots, N_1 - 1$ and $\forall k_y = 0, 1, 2, \dots, N_2 - 1$, with $w(0) = 1$ and $w(k > 0) = \sqrt{2}$ to obtain an orthonormal transform:

$$D_{k_x, k_y} = \frac{w(k_x)w(k_y)}{\sqrt{N_1 N_2}} \sum_{x=0}^{N_1-1} \sum_{y=0}^{N_2-1} I_{x,y} \cos\left[\frac{\pi}{N_1} \left(x + \frac{1}{2}\right) k_x\right] \cos\left[\frac{\pi}{N_2} \left(y + \frac{1}{2}\right) k_y\right].$$

When we plot the DCT spectrum, we depict the DCT coefficients as a heatmap. Intuitively, the magnitude of each coefficient is a measure of how much the corresponding spatial frequency contributed to the overall image. The horizontal direction corresponds to frequencies in the x direction, while the vertical direction corresponds to frequencies in the y direction.

In practice we compute the 2D-DCT as a product of two 1D-DCTs, i.e., for images we first compute a DCT along the columns and then a DCT along the rows. This results in the top left corner of the heatmap corresponding to low frequencies (k_x and k_y close to zero), while the right bottom corner corresponds to high frequencies (k_x and k_y close to $N_1 - 1$ and $N_2 - 1$, respectively). Due to the energy compaction property of the DCT, the coefficients drop very quickly in magnitude when moving to high frequencies, thus, we log-scale the coefficients before plotting. All plots are computed for gray-scale images, produced using standard gray-scale transformations (i.e., a weighted average over the color channels). We also computed statistics for each color channel separately, which are consistent with the findings for gray-scale images. These can be found in the appendix.

3.2. Investigating Generated Images in the Frequency Domain

We start with examining our introductory example, i.e., images from the website whichfaceisreal.com. The images are either from the Flickr-Faces-HQ data set (FFHQ) or from a set generated by StyleGAN (Karras et al., 2019). In Figure 1, we visualize the frequency statistics of the data set by plotting the means of the corresponding spectra over the sets. As a reference, we include a sample from each data set. In the image domain, both samples look similar, however, in the frequency domain, one can easily spot multiple clearly visible artifacts for the generated images.

¹For simplicity, we omit the color channels and treat images as matrices, not as tensors.

The spectrum of the FFHQ images represents a regular spectrum of DCT coefficients. Multiple studies (e.g. see Burton & Moorhead, 1987; Tolhurst et al., 1992; Field, 1987; 1999) have observed that the average power spectra of natural images tend to follow a $\frac{1}{f^\alpha}$ curve, where f is the frequency along a given axis and $\alpha \sim 2$ (see Figure 2(a) from Torralba & Oliva, 2003). The low frequencies (in the upper left corner of the heatmap) contribute the most to the image, and the contribution is gradually decreasing as we approach the higher frequencies (lower right corner). Intuitively, if a group of neighboring pixels contains similar values, i.e., they form an isochromatic area in the image, one can approximate those with a sum of low frequency functions. However, if there is a sudden change in the values, e.g., corresponding to an edge in the images, one has to use higher frequency functions to achieve a good approximation. Therefore, since most pixels in images are correlated to each other, i.e., colors mostly change gradually, large parts of the image can be approximated well by using low-frequency functions.

The StyleGAN-generated images, however, exhibit artifacts throughout the spectrum. In comparison to the spectra of natural images, StyleGAN-generated images contain strong high frequencies components (visible as high values in the lower right corner), as well as generally higher magnitudes throughout the spectrum. Especially notably is the grid-like pattern scattered throughout, also clearly noticeable in the top right (highest frequencies in x direction) and lower left corner (highest frequencies in y direction).

To analyze if this pattern in the spectral domain is a common occurrence for different GAN types, or simply a fault specific to the StyleGAN instance we studied, we selected four different architectures, namely BigGAN (Brock et al., 2019), ProGAN (Karras et al., 2018), StyleGAN (Karras et al., 2019), and SN-DCGAN (Miyato et al., 2018). Note that all of them were under the top-ten entries in the recent Kaggle competition on generating images of dogs (Kaggle, 2019). In this competition the participants were required to upload 10,000 samples from their respective GAN instance. For each architecture, we downloaded and analyzed the corresponding samples, as well as the training data (Khosla et al., 2011).

We show the mean of the spectrum over the samples of each GAN and the training data in Figure 2. As discussed, statistics of natural images have been found to follow particular regularities. Like natural images, the DCT coefficients of the GAN-generated images decrease rapidly towards high frequencies. However, the spectral images often show a grid-like pattern, which indicates a structural problem of the way GANs generate images that we explore further.



Figure 1: **A side-by-side comparison of real and generated faces in image and frequency domain.** The left side shows an example and the spectrum of the FFHQ data set. The right side shows an example and the spectrum of a data set sampled from StyleGAN trained on FFHQ. We plot the mean of the DCT spectrum. We estimate $\mathbb{E}[\mathcal{D}(I)]$ by averaging over 10,000 images.

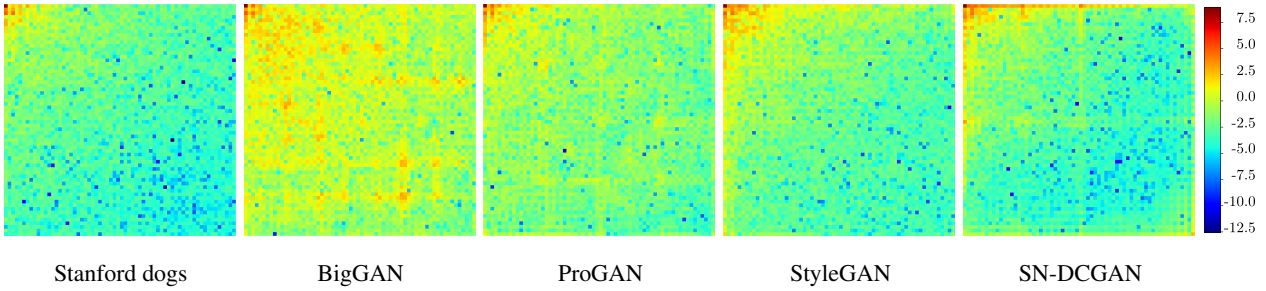


Figure 2: **The spectra of different neural networks trained on the Stanford dog data set.** The left-most heatmap depicts the spectrum of the Stanford dog data set. The rest depicts spectra of different neural networks. We plot the mean of the DCT spectrum. We estimate $\mathbb{E}[\mathcal{D}(I)]$ by averaging over 10,000 images.

3.3. Upsampling

We hypothesize that the artifacts found for GAN-generated images in the frequency domain stem from upsampling operations. We make this more concrete in the following. With training the generator, GANs learn a mapping from a low-dimensional latent space to the higher-dimensional data space. In practice, the dimensionality of the latent space is much lower than the dimensionality of the data space, e.g., the generator of the StyleGAN-instance which generated the images presented in Figure 1 defines a mapping $G: \mathbb{R}^{100} \rightarrow \mathbb{R}^{1024 \times 1024}$. In typical GAN architectures, the latent vector gets successively upsampled until it reaches the final output dimension.

Previous work has already linked upsampling operations to causing grid-like patterns in the image domain (Odena et al., 2016). Recognizing this, the architecture of both the generator-network and the discriminator-network shifted from using strided transposed convolution (e.g., employed in DCGAN (Radford et al., 2016), CramerGAN (Bellemare et al., 2017), CycleGAN (Zhu et al., 2017), MMDGAN (Bińkowski et al., 2018), and SN-DCGAN (Miyato et al., 2018)) to using traditional upsampling methods—like nearest neighbor or bilinear upsampling (Gonzalez & Woods, 1992)—followed by a convolutional

layer (e.g., employed in BigGAN (Brock et al., 2019), ProGAN (Karras et al., 2018), and StyleGAN (Karras et al., 2019)).

Moreover, both upsampling and downsampling operations have recently been linked to compromising shift invariance in neural networks, i.e., they cause classifier predictions to vary dramatically due to a simple one-pixel shift in the input image (Azulay & Weiss, 2018). Recently, Zhang (2019) proposed to use low-pass filtering after convolution and pooling layers to mitigate some of these effects.

We investigate how different upsampling strategies affect the DCT spectrum. Typically, we want to double the dimensionality of an image. When doing so, we have to fill in the blanks. A simple method is to simply copy the nearest pixel over (nearest-neighbor upsampling; for a visual representation see Odena et al., 2016). However, this is known to cause artifacts. Thus, a range of different techniques have been invented throughout the past few years to minimize these detrimental effects (Gonzalez & Woods, 1992). In our analysis, we investigate the effect of three different upsampling techniques:

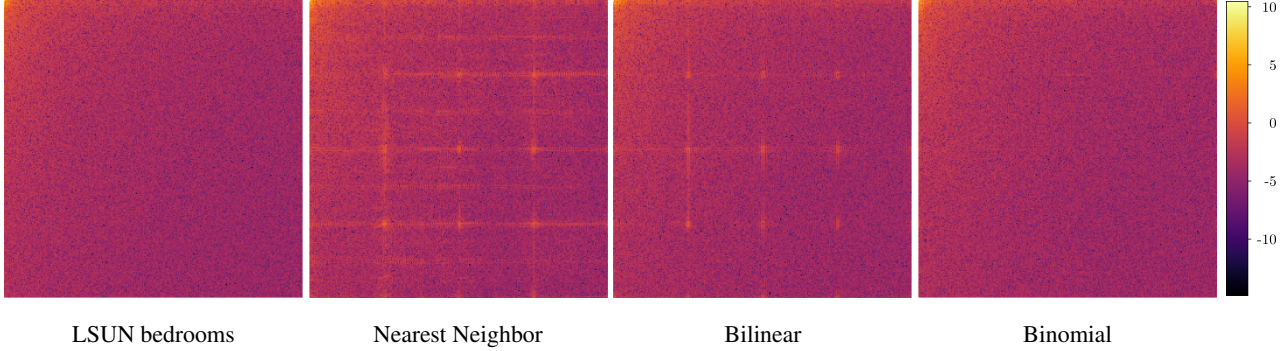


Figure 3: **The frequency spectrum resulting from different upsampling techniques.** We plot the mean of the DCT spectrum. We estimate $\mathbb{E}[\mathcal{D}(I)]$ by averaging over 10,000 images sampled from the corresponding network or the training data.

- **Nearest Neighbor:** The missing pixels in the upsampled image are approximated by copying the nearest pixel.
- **Bilinear:** Similar to nearest neighbor, however, after copying the pixel values, the upsampled image is convolved with an anti-aliasing kernel (the filter $[1, 2, 1]^2$)². This strategy is employed in the original StyleGAN.
- **Binomial:** We follow [Zhang \(2019\)](#) and test the Binomial-5 kernel (i.e., the application of the filter $[1, 4, 6, 4, 1]$) as a replacement for the bilinear kernel.

We trained three different versions of StyleGAN on the LSUN bedrooms ([Yu et al., 2015](#)) dataset: in one, we kept the standard bilinear upsampling strategy, and in two, we replaced it by nearest-neighbor upsampling and binomial upsampling, respectively. We train at a resolution of 256×256 , using the standard model and settings provided in the StyleGAN repository ([Karras et al., 2019](#)).

We plot the average spectra over 10,000 samples for each model, the results are shown in Figure 3. As expected, with more elaborated upsampling techniques and with a larger size of the employed kernel, the spectral images become smoother and the artifacts less severe. These findings are in line with our hypothesis that the artifacts are caused by upsampling operations.

4. Frequency-based Deep-Fake Recognition

In the following, we describe our experiments to demonstrate the effectiveness of the frequency domain for differentiating GAN-generated images. In a first experiment, we show that DCT-transformed images are fully linearly separable, while classification on raw pixels requires non-linear models. Further, we verify that our model utilizes the artifacts discovered in Section 3.2. Then, we recreate

²Note that for brevity, we list the 1D-variant of the anti-aliasing kernel; in practice, we generate the 2D-variant as the outer product: $m m^T$, where m is the corresponding kernel.

the experiments by [Yu et al. \(2019a\)](#) and show how we can utilize the frequency domain to match generated images to their underlying architecture, demonstrating that we can both achieve higher accuracy while utilizing fewer parameters in our models. Finally, we investigate how our classifier behaves when confronted with common image perturbations.

All experiments in this chapter were performed on a server running Ubuntu 18.04, with 192 GB RAM, an Intel Xeon Gold 6230, and four Nvidia Quadro RTX 5000.

4.1. Detecting Fake Images

First, we want to demonstrate that making use of frequency information allows to efficiently separate real from fake images. We consider our introductory example, i.e., aim at distinguishing real images from the FFHQ data set and fake images generated by StyleGAN. As discussed in Section 3, in the frequency domain, the images show severe artifacts. These artifacts make it easy to use a simple linear classifier. To demonstrate this, we perform a ridge regression on real and generated images, after applying a DCT. For comparison, we also perform ridge regression on the original data representation.

Experiment Setup We sample 16,000 images from both the training data and the generator of the StyleGAN, respectively. We split each set into 10,000 training, 1,000 validation and 5,000 test images, resulting in a training set of 20,000, a validation set of 2,000, and a test set of 10,000 samples. For training a model on samples in the image domain, we normalize the pixel values to the range $[-1, 1]$. In the frequency domain, we first convert the images using DCT, then log-scale the coefficients and, finally, normalize them by removing the mean and scaling to unit variance. We optimize the regression model using the Adam optimizer ([Kingma & Ba, 2015](#)) with a learning rate of 0.001, minimizing the binary cross-entropy with l_2 regularization.

Table 1: **Ridge regression performed on FFHQ data set.** We report the accuracy on the test set. We also report the gain in accuracy when training in the frequency domain instead of using raw pixels. Best score is highlighted in **bold**.

Method	Accuracy	Gain
Ridge-Regression-Pixel	75.78 %	
Ridge-Regression-DCT	100.00 %	+ 24.22 %

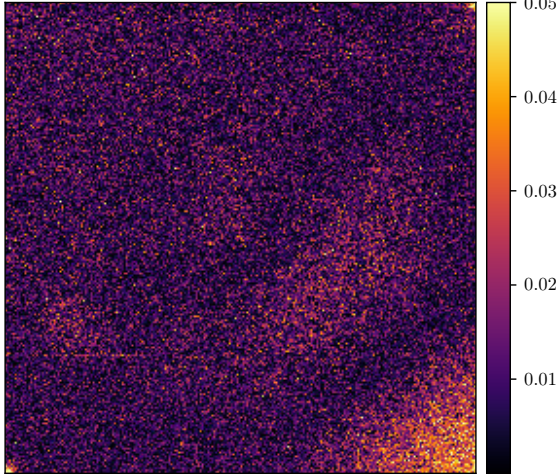


Figure 4: **A heatmap of which frequencies the LASSO-regression uses.** We extracted the weight vector of the regression classifier and mapped it back to the corresponding frequencies. We plot the absolute value of the individual weights and clip their maximum value to 0.05 for better visibility. Note the general focus towards higher frequencies, as well as the top right and lower left corner.

We select the regularization factor λ via grid search from $\lambda \in \{1^{-1}, 1^{-2}, 1^{-3}, 1^{-4}\}$ on the validation data, picking the one with the best score.

Results The results of our experiments are listed in Table 1, where we report the classification accuracy of the test set. As depicted in Figure 1, StyleGAN generates convincing face images, which are able to fool humans. However, they seem to exhibit consistent patterns, since even the simple linear classifier reaches a non-trivial accuracy in the image domain. In the frequency domain, however, we can perfectly separate the data set, with a classification accuracy of 100 % on the test set.

To verify that the classifier indeed utilizes the upsampling artifacts for its decision, we perform an additional experiment: we train a logistic regression classifier with l_1 (LASSO) penalty on the data set. We then extract the corresponding weight vector, map it back to the corresponding frequencies, and plot its absolute values as a heatmap in Figure 4. The penalty forces weights to zero which play a minor role in the classification, i.e., the high coefficients correspond to

the frequencies which impact the decision the most. The classifier mostly concentrates on the higher frequencies, as well as on the corners with the highest frequencies in the x and y direction. In context with Figure 1, this makes sense, since compared to the real spectrum, the generated images diverge most in the higher frequencies (real images contain very little energy here) and the grid-like points. As discussed in Section 3.2, the power spectra of natural images falls off towards higher-frequencies. Thus, these areas provide a strong signal to the classifier.

4.2. Source Identification

The experiments described in this section are based on Yu et al. (2019a)’s approach, and investigate how easy a generated image’s underlying architecture can be classified: Yu et al. trained four different GANs (ProGAN (Karras et al., 2018), SN-DCGAN (Miyato et al., 2018), CramerGAN (Bellemare et al., 2017), and MMDGAN (Bińkowski et al., 2018)) on the CelebA (Liu et al., 2015) and LSUN bedrooms dataset (Yu et al., 2015) and generated images from all models. Based on these images, a classification has been performed that assigned each image to the corresponding subset, i.e., either real, ProGAN, SN-DCGAN, CramerGAN, or MMDGAN.

Experiment Setup The experiments are conducted on images of resolution 128×128 . We converted both data set (i.e., celebA and LSUN bedrooms) as per the specifications provided by Yu et al. (2019b) . For each data set, we utilize their pre-trained models (Yu et al., 2019b) to sample 150,000 images from each GAN, and take another 150,000 real images randomly sampled from the underlying training data set. We then partition these samples into 100,000 training, 20,000 validation and 30,000 test images, resulting in a combined set of 500,000 training, 100,000 validation and 150,000 test images. We analyze the performance of different classifiers trained both on the images in their original representation (i.e., raw pixels) and after applying DCT: K-nearest-neighbor, Eigenfaces (Sirovich & Kirby, 1987)), a CNN-based classifier developed by Yu et al. (2019a), and a steganalysis method based on photo-response non-uniformity (PRNU) patterns by Marra et al. (2019). These patterns also build on frequency information and utilizes high-pass filtered images to extract residuals information common to specific generators.

Moreover, we trained a shallow CNN, with only four convolution layers, to demonstrate that frequency information can significantly reduce the needed computationally resources. Details on the architecture can be found in the appendix. Yu et al. used a very large CNN with roughly 9 million parameters. In contrast, our CNN only utilizes around 170,000 parameters ($\sim 1.9\%$). During training, we utilize the validation set for hyperparameter tuning and employ

Table 2: **The results of the source identification.** We report the accuracy on the test set. For each method we also report the gain in accuracy when using the DCT-variant of the classifier. Best score is highlighted in **bold**.

Method	LSUN	Gain	CelebA	Gain
kNN	39.83 %		28.80 %	
kNN-DCT	80.62 %	+ 40.79 %	69.15 %	+ 40.35 %
Eigenfaces	42.47 %		49.59 %	
Eigenfaces-DCT	88.62 %	+ 46.15 %	83.27 %	+ 33.68 %
PRNU Marra et al.	64.09 %		80.32 %	
CNN Yu et al.	98.33 %		99.70 %	
CNN Yu et al.-DCT	99.61 %	+ 1.28 %	99.91 %	+ 0.21 %
CNN-Pixel	98.95 %		97.80 %	
CNN-DCT	99.64 %	+ 0.69 %	99.07 %	+ 1.27 %

early stopping. We trained on log-scaled and normalized DCT coefficients. For raw pixel, we scaled the values to the range $[-1, 1]$, except for the PRNU-based method, which operates directly on image data.

For training our CNN, we use the Adam optimizer, with a learning rate of 0.001 and a batch size of 1024, minimizing the cross-entropy loss of the model. For Yu et al.’s CNN we used the parameters specified in their repository (Yu et al., 2019b). We train their network for 8,000 mini-batch steps. During first tests we discovered their network usually converges at around 4,000 steps, thus, we doubled the number of steps for the final evaluation and picked the best performing instance (measured on the validation set). We also trained a variant of their classifier on DCT-transformed images. This version usually converges around step 30, however, we are conservative and train for 1,000 steps.

For the PRNU classifier, we utilize the implementation of Bondi & Bonettini (2019). We set the wavelet decomposition level l to 4 and the estimated noise power σ to 0.95 after performing a grid search for $l \in \{1, 2, 3, 4\}$ and $\sigma \in \{0.05, 0.1, \dots, 1\}$. For the Eigenfaces-based classifier, we use Principal Component Analysis (PCA) to reduce the dimensionality to a variance threshold of 0.95 and train a linear Support Vector Machine (SVM) on the transformed training data. Finally, for the kNN classifier we perform a grid search over the number of considered neighbors $k \in \{1, 2^1 + 1, \dots, 2^{10} + 1\}$. We perform the hyperparameter search for each data set separately, picking the best result on the corresponding validation set. As the PRNU fingerprint algorithm does not require a large amount of training data (Marra et al., 2019) and scaling more traditional methods to such large data sets is notoriously hard (i. e., kNN and Eigenfaces), we use a subset of 100,000 training samples and report the accuracy for the full test set.

Results The results of our experiments are presented in Table 2. We report the accuracy computed over the test set.

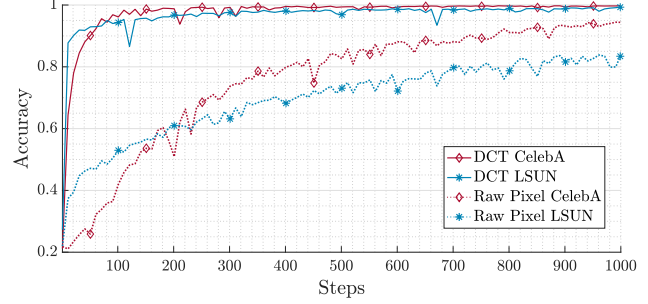


Figure 5: **Validation accuracy for the CCN-classifier by Yu et al.** We report the validation accuracy during training for the first 1,000 gradient steps.

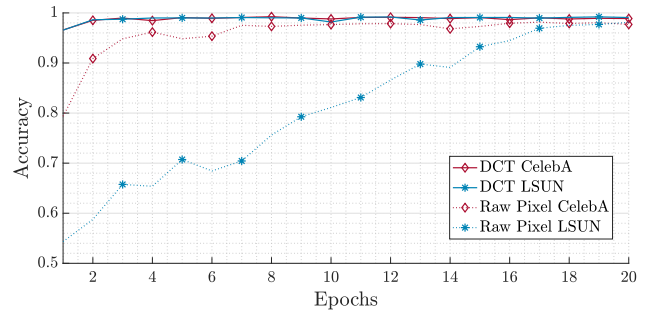


Figure 6: **Validation accuracy for our CNN-classifier.** We report the validation accuracy during training for the first 20 epochs.

For each method, we additionally report the gain in accuracy when trained on DCT coefficients.

The use of the frequency domain significantly improves the performance of all tested classifiers, which is in line with our findings from the previous sections. The simpler techniques improve the most, with kNN gaining a performance boost of roughly 40 % and Eigenfaces improving by 46.15 % and 33.68 %, respectively. Our shallow CNN already achieves high accuracy when it is trained on raw pixels (CNN-Pixel), but it still gains a performance boost (+0.69 % and 1.27 %, respectively). The CNN employed by Yu et al. (2019a) mirrors the result of our classifier. Additionally, it seems to be important to utilize the entire frequency spectrum, since the PRNU-based classifier by Marra et al. (2019) achieves much lower accuracy.

As an additional evidence of the effectiveness of classification in the frequency domain, we plot the validation accuracy during training for both the CNN classifier by Yu et al. (2019a), as well as for our own (Figure 5 and Figure 6, respectively). Since we use the Adam optimizer, we are not influenced by the learning rate. For both classifier across both CelebA and LSUN, the DCT variant of the classifier converges significantly faster.

Table 3: **Results of common image perturbations on LSUN bedrooms.** We report the accuracy on the test set. Best score is highlighted in **bold**.

	Blur		Cropped		Compression		Noise		Combined	
	CD	PD								
CNN-Pixel	60.56 %	88.23 %	74.49 %	97.82 %	68.66 %	78.67 %	59.51 %	78.18 %	65.98 %	73.32 %
CNN-DCT	61.42 %	93.61 %	83.52 %	98.83 %	71.86 %	94.83 %	48.99 %	89.56 %	67.76 %	90.77 %

CD: Clean Data; PD: Perturbed Data

4.3. Resistance Against Common Image Perturbations

We also evaluate the resistance of our classifier against common image perturbations, namely: blurring, cropping, compression, adding random noise, as well as a combination of all of them.

Experiment Setup When creating the perturbed data with one kind of perturbation, for each data set we iterate through all images and apply the perturbation with a probability of 50 %. This creates new data sets with about half the images corrupted, these again get divided into train/validation/tests sets, accuracy is reported for the test set. For generating a data set with a combination of different perturbations, we cycle through the different corruptions in the order: blurring, cropping, compression, noise; and apply these with a probability of 50 %. The corruptions are described in the following:

- **Blurring** applies Gaussian filtering with a kernel size randomly sampled from (3, 5, 7, 9).
- **Cropping** randomly crops the image along both axes. The percentage to crop is sampled from $U(5, 20)$. The cropped image is upsampled to its original resolution.
- **Compression** applies JPEG compression, the remaining quality factor is sampled from $U(10, 75)$.
- **Noise** adds i.i.d. Gaussian Noise to the image. The variance of the Gaussian distribution is randomly sampled from $U(5.0, 20.0)$.

We additionally evaluate how well we can defend against common image perturbations utilizing adversarial training. We retrain the network with a training set that has also been altered by image perturbations.

Results The results are presented in Table 3. The column *CD* refers to the performance of the corresponding classifier trained on clean data and evaluated on perturbed test data. In the column *PD*, we depict the performance when trained on training data which is also perturbed. Overall, our results show that the DCT variants of the classifiers perform better in all cases but adding noise.

5. Conclusion and Discussion

In this paper, we have provided a comprehensive analysis on the frequency spectrum exhibited by images generated from different GAN architectures. Our main finding is that *all* spectra contain artifacts common across architectures, data sets, and resolutions. Speculating that these artifacts stem from upsampling operations, we experimented with different upsampling techniques and showed that they confirm our hypothesis. We than have demonstrated that the frequency spectrum can be used to efficiently and accurately separate real from deep fake images. We have found that the frequency domain both helps in enhancing simple (linear) models, as well as, more complex CNN-based methods, while simultaneously yielding better resistance against image perturbations. Compared to hand-crafted, frequency-based methods, we discovered that the entire frequency spectrum can be utilized to achieve much higher performance. We argue that our method will remain usable in the future because it relies on a fundamental property of today’s GANs, i.e., the mapping from low dimensional latent space to a higher dimensional data space.

One suitable approach to mitigate this problem could be to remove upsampling methods entirely. First, this would remove the advantages of having a compact latent space altogether. Second, an instance of StyleGAN used to generate the pictures depicted in Figure 1 already needs 26.2M (Karras et al., 2019) parameters. Removing the low-dimensional layers and only training at full resolution seems infeasible, at least for the foreseeable future.

Another approach is to train GANs to generate consistent image spectra. We experimented with both introducing a second DCT-based discriminator, as well as, regularizing the generator’s loss function with a DCT-based penalty. Unfortunately, neither approach led to better results. Either the penalty or the second discriminator were weighted too weak and had no effect, or the DCT-based methods dominated and led to training collapse. Since GAN training is inherently unstable, we speculate that these alternatives might need considerable effort. We leave the exploration of these as an interesting question for future work.

Acknowledgements We would like to thank our colleagues Cornelius Aschermann, Steffen Zeiler, Sina Däubener, and Philipp Görz for their valuable feedback and fruitful discussions. This work was supported by the Deutsche Forschungsgemeinschaft (DFG, German Research Foundation) under Germany’s Excellence Strategy – EXC-2092 CASA – 390781972.

References

Arjovsky, M., Chintala, S., and Bottou, L. Wasserstein gan. In *International Conference on Machine Learning (ICML)*, 2017.

Azulay, A. and Weiss, Y. Why do deep convolutional networks generalize so poorly to small image transformations? *arXiv preprint arXiv:1805.12177*, 2018.

Bappy, J. H., Roy-Chowdhury, A. K., Bunk, J., Nataraj, L., and Manjunath, B. Exploiting spatial structure for localizing manipulated image regions. In *IEEE International Conference on Computer Vision (ICCV)*, 2017.

Bayar, B. and Stamm, M. C. A deep learning approach to universal image manipulation detection using a new convolutional layer. In *ACM Workshop on Information Hiding and Multimedia Security*, 2016.

Bellemare, M. G., Danihelka, I., Dabney, W., Mohamed, S., Lakshminarayanan, B., Hoyer, S., and Munos, R. The cramer distance as a solution to biased wasserstein gradients. *arXiv preprint arXiv:1705.10743*, 2017.

Bestagini, P., Milani, S., Tagliasacchi, M., and Tubaro, S. Local tampering detection in video sequences. In *IEEE International Workshop on Multimedia Signal Processing (MMSP)*, 2013.

Bińkowski, M., Sutherland, D. J., Arbel, M., and Gretton, A. Demystifying mmd gans. In *International Conference on Learning Representations (ICLR)*, 2018.

Bondi, L. and Bonettini, N. polimi-ispl/prnu-python: v.1.2. <https://doi.org/10.5281/zenodo.2554965>, February 2019.

Brock, A., Donahue, J., and Simonyan, K. Large scale GAN training for high fidelity natural image synthesis. In *International Conference on Learning Representations (ICLR)*, 2019.

Burton, G. J. and Moorhead, I. R. Color and spatial structure in natural scenes. *Applied optics*, 1987.

Cozzolino, D., Poggi, G., and Verdoliva, L. Recasting residual-based local descriptors as convolutional neural networks: an application to image forgery detection. In *ACM Workshop on Information Hiding and Multimedia Security*, 2017.

Field, D. J. Relations between the statistics of natural images and the response properties of cortical cells. *Journal of the Optical Society of America. A, Optics and image science*, 1987.

Field, D. J. Wavelets, vision and the statistics of natural scenes. *Philosophical Transactions of the Royal Society of London. Series A: Mathematical, Physical and Engineering Sciences*, 1999.

Fridrich, J. Digital image forensics. *IEEE Signal Processing Magazine*, 2009.

Fried, O., Tewari, A., Zollhöfer, M., Finkelstein, A., Shechtman, E., Goldman, D. B., Genova, K., Jin, Z., Theobalt, C., and Agrawala, M. Text-based editing of talking-head video. *ACM Transactions on Graphics (TOG)*, 2019.

Gonzalez, R. C. and Woods, R. E. *Digital Image Processing*. Pearson, 1992.

Goodfellow, I., Pouget-Abadie, J., Mirza, M., Xu, B., Warde-Farley, D., Ozair, S., Courville, A., and Bengio, Y. Generative adversarial nets. In *Advances in Neural Information Processing Systems (NeurIPS)*, 2014.

Gulrajani, I., Ahmed, F., Arjovsky, M., Dumoulin, V., and Courville, A. C. Improved training of wasserstein gans. In *Advances in Neural Information Processing Systems (NeurIPS)*, 2017.

Hao, K. The biggest threat of deepfakes isn’t the deepfakes themselves. *MIT Technology Review*, 2019.

Kaggle. Generative dog images - experiment with creating puppy pics. <https://www.kaggle.com/c/generative-dog-images>, 2019.

Karras, T., Aila, T., Laine, S., and Lehtinen, J. Progressive growing of GANs for improved quality, stability, and variation. In *International Conference on Learning Representations (ICLR)*, 2018.

Karras, T., Laine, S., and Aila, T. A style-based generator architecture for generative adversarial networks. In *IEEE Conference on Computer Vision and Pattern Recognition (CVPR)*, 2019.

Khosla, A., Jayadevaprakash, N., Yao, B., and Fei-Fei, L. Novel dataset for fine-grained image categorization. In *First Workshop on Fine-Grained Visual Categorization, IEEE Conference on Computer Vision and Pattern Recognition (CVPR)*, 2011.

Kingma, D. P. and Ba, J. Adam: A method for stochastic optimization. In *International Conference on Learning Representations (ICLR)*, 2015.

Kumar, K., Kumar, R., de Boissiere, T., Gestin, L., Teoh, W. Z., Sotelo, J., de Brébisson, A., Bengio, Y., and Courville, A. C. Melgan: Generative adversarial networks for conditional waveform synthesis. In *Advances in Neural Information Processing Systems (NeurIPS)*, 2019.

Liu, Z., Luo, P., Wang, X., and Tang, X. Deep learning face attributes in the wild. In *IEEE International Conference on Computer Vision (ICCV)*, December 2015.

Lukáš, J., Fridrich, J., and Goljan, M. Digital camera identification from sensor pattern noise. *IEEE Transactions on Information Forensics and Security*, 2006.

Lyu, S. Natural image statistics in digital image forensics. In *Digital Image Forensics*, pp. 239–256. Springer, 2013.

Marra, F., Gragnaniello, D., Cozzolino, D., and Verdoliva, L. Detection of gan-generated fake images over social networks. In *IEEE Conference on Multimedia Information Processing and Retrieval (MIPR)*, 2018.

Marra, F., Gragnaniello, D., Verdoliva, L., and Poggi, G. Do gans leave artificial fingerprints? In *IEEE Conference on Multimedia Information Processing and Retrieval (MIPR)*, 2019.

McCloskey, S. and Albright, M. Detecting gan-generated imagery using color cues. *arXiv preprint arXiv:1812.08247*, 2018.

Mirza, M. and Osindero, S. Conditional generative adversarial nets. *arXiv preprint arXiv:1411.1784*, 2014.

Miyato, T., Kataoka, T., Koyama, M., and Yoshida, Y. Spectral normalization for generative adversarial networks. *International Conference on Learning Representations (ICLR)*, 2018.

Mo, H., Chen, B., and Luo, W. Fake faces identification via convolutional neural network. In *ACM Workshop on Information Hiding and Multimedia Security*, 2018.

Nataraj, L., Mohammed, T. M., Manjunath, B., Chandrasekaran, S., Flenner, A., Bappy, J. H., and Roy-Chowdhury, A. K. Detecting gan generated fake images using co-occurrence matrices. *Electronic Imaging*, 2019.

Odena, A., Dumoulin, V., and Olah, C. Deconvolution and checkerboard artifacts. *Distill*, 2016.

Petzka, H., Fischer, A., and Lukovnicov, D. On the regularization of wasserstein gans. In *International Conference on Learning Representations (ICLR)*, 2018.

Radford, A., Metz, L., and Chintala, S. Unsupervised representation learning with deep convolutional generative adversarial networks. In *International Conference on Learning Representations (ICLR)*, 2016.

Razavi, A., van den Oord, A., and Vinyals, O. Generating diverse high-fidelity images with vq-vae-2. In *Advances in Neural Information Processing Systems (NeurIPS)*, 2019.

Salimans, T., Goodfellow, I., Zaremba, W., Cheung, V., Radford, A., and Chen, X. Improved techniques for training gans. In *Advances in Neural Information Processing Systems (NeurIPS)*, 2016.

Simonite, T. Artificial intelligence is coming for our faces. *Wired*, 2019.

Sirovich, L. and Kirby, M. Low-dimensional procedure for the characterization of human faces. *Journal of the Optical Society of America. A, Optics and image science*, 1987.

Song, L., Wu, W., Qian, C., He, R., and Loy, C. C. Everybody's talkin': Let me talk as you want. *arXiv preprint arXiv:2001.05201*, 2020.

Tariq, S., Lee, S., Kim, H., Shin, Y., and Woo, S. S. Gan is a friend or foe? a framework to detect various fake face images. In *ACM/SIGAPP Symposium on Applied Computing*, 2019.

Thompson, N. and Lapowsky, I. How russian trolls used meme warfare to divide america. *Wired*, 2017.

Tolhurst, D., Tadmor, Y., and Chao, T. Amplitude spectra of natural images. *Ophthalmic and Physiological Optics*, 1992.

Torralba, A. and Oliva, A. Statistics of natural image categories. *Network: computation in neural systems*, 2003.

Valle, R., Cai, W., and Doshi, A. Tequilagan: How to easily identify gan samples. *arXiv preprint arXiv:1807.04919*, 2018.

van den Oord, A., Vinyals, O., et al. Neural discrete representation learning. In *Advances in Neural Information Processing Systems (NeurIPS)*, 2017.

Wen-Hsiung Chen, Smith, C., and Fralick, S. A fast computational algorithm for the discrete cosine transform. *IEEE Transactions on Communications*, 1977.

West, J. and Bergstrom, C. Which face is real? <http://www.whichfaceisreal.com>, 2019.

Yu, F., Zhang, Y., Song, S., Seff, A., and Xiao, J. Lsun: Construction of a large-scale image dataset using deep learning with humans in the loop. *arXiv preprint arXiv:1506.03365*, 2015.

Yu, N., Davis, L. S., and Fritz, M. Attributing fake images to gans: Learning and analyzing gan fingerprints. In *IEEE International Conference on Computer Vision (ICCV)*, 2019a.

Yu, N., Davis, L. S., and Fritz, M. Attributing fake images to gans: Learning and analyzing gan fingerprints. <https://github.com/ningyu1991/GANFingerprints>, 2019b.

Zhang, R. Making convolutional networks shift-invariant again. In *International Conference on Machine Learning (ICML)*, 2019.

Zhou, P., Han, X., Morariu, V. I., and Davis, L. S. Learning rich features for image manipulation detection. In *IEEE International Conference on Computer Vision (ICCV)*, 2018.

Zhu, J.-Y., Park, T., Isola, P., and Efros, A. A. Unpaired image-to-image translation using cycle-consistent adversarial networks. In *IEEE International Conference on Computer Vision (ICCV)*, 2017.

Appendix

In this appendix we present additional statistics separated into each color channel, as well as details on our classifier architecture. Note the statistics split into color channels are consistent with the ones computed over gray-scale images. Thus, for brevity, we only depict split statistics for the Stanford data set.

A. Network Architecture

For training our CNN we use the Adam optimizer, with an initial learning rate of 0.001, $\beta_1 = 0.9$, $\beta_2 = 0.999$ and $\epsilon = 1^{-7}$, which are the standard parameters for a TensorFlow implementation. We did some experiments with different settings, but none seem to influence the training substantially, so we kept the standard configuration. We train with a batch size of 1024. Again, we experimented with lower batch sizes, which did not influence the training. Thus, we simply picked the largest batch size our GPUs allowed for.

Input (128x128x3)
Conv 3x3 (128x128x3)
Conv 3x3 (128x128x8)
Average-Pool 2x2 (64x64x8)
Conv 3x3 (64x64x16)
Average-Pool 2x2 (32x32x16)
Conv 3x3 (32x32x32)
Dense (5)

Table 4: The network architecture for our simply CNN. We report the size of each layer in (brackets).

B. Color Channel Statistics

We plot the mean of the DCT spectrum of the Stanford dog data set and images generated by different instances of GANs (BigGAN, ProGAN, StyleGAN, SN-DCGAN) trained upon it. We estimate $\mathbb{E}[\mathcal{D}(I)]$ by averaging over 10,000 images.

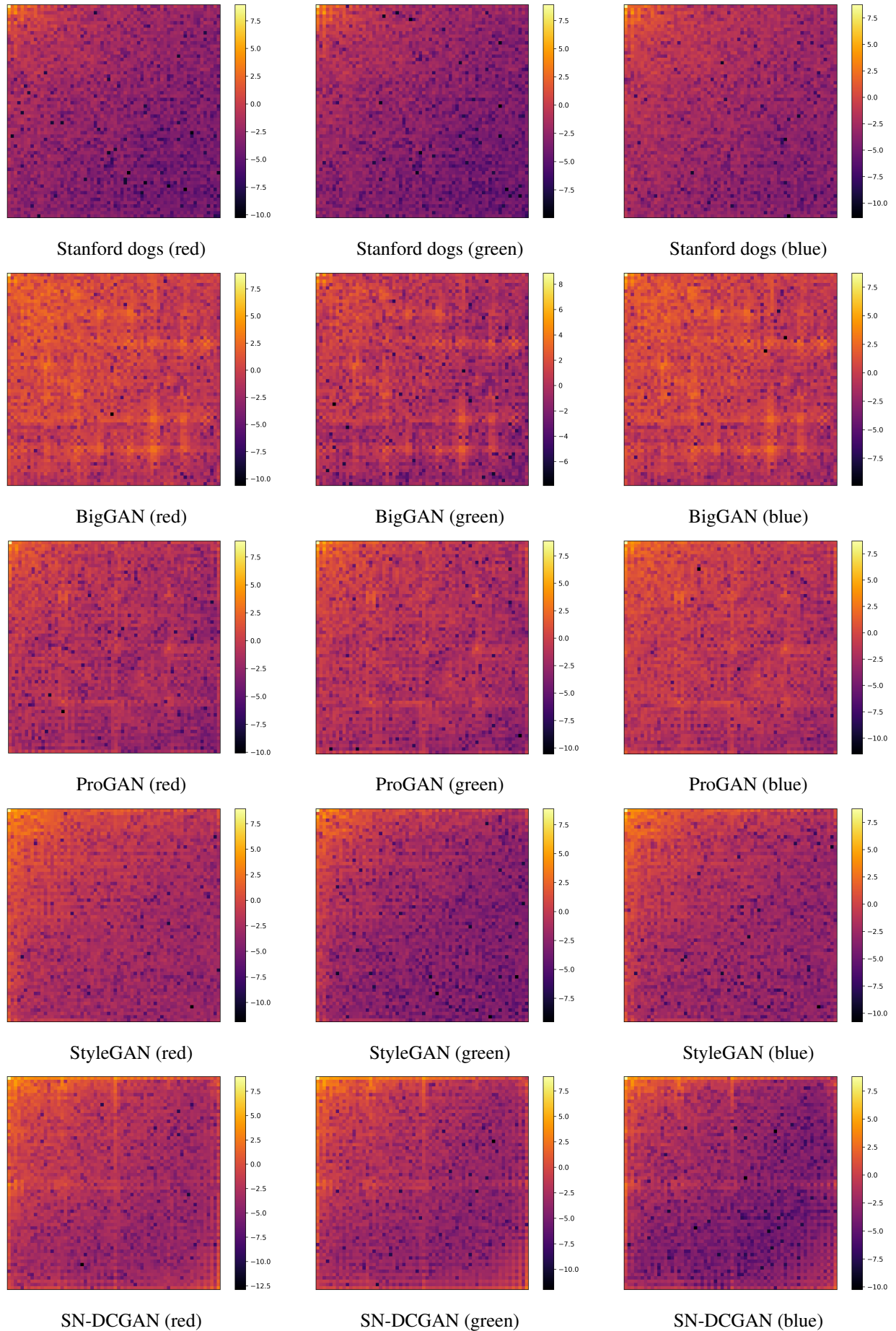


Figure 7: The frequency spectrum of sample sets generated by different types of GANs trained on the Stanford dog data set (separated into color channels)